ORIGINAL PAPER

Nanogeochemistry of hydrothermal magnetite

Artur P. Deditius[1] · Martin Reich[2,3] · Adam C. Simon[4] · Alexandra Suvorova[5] · Jaayke Knipping[4] ·
Malcolm P. Roberts[5] · Sergey Rubanov[6] · Aaron Dodd[5] · Martin Saunders[5]

Abstract

Magnetite from hydrothermal ore deposits can contain up to tens of thousands of parts per million (ppm) of elements such as Ti, Si, V, Al, Ca, Mg, Na, which tend to either structurally incorporate into growth and sector zones or form mineral micro- to nano-sized particles. Here, we report micro- to nano-structural and chemical data of hydrothermal magnetite from the Los Colorados iron oxide–apatite deposit in Chile, where magnetite displays both types of trace element incorporation. Three generations of magnetites (X–Z) were identified with concentrations of minor and trace elements that vary significantly: SiO_2, from below detection limit (bdl) to 3.1 wt%; Al_2O_3, 0.3–2.3 wt%; CaO, bdl–0.9 wt%; MgO, 0.02–2.5 wt%; TiO_2, 0.1–0.4 wt%; MnO, 0.04–0.2 wt%; Na_2O, bdl–0.4 wt%; and K_2O, bdl–0.4 wt%. An exception is V_2O_3, which is remarkably constant, ranging from 0.3 to 0.4 wt%. Six types of crystalline nanoparticles (NPs) were identified by means of transmission electron microscopy in the trace element-rich zones, which are each a few micrometres wide: (1) diopside, (2) clinoenstatite; (3) amphibole, (4) mica, (5) ulvöspinel, and (6) Ti-rich magnetite. In addition, Al-rich nanodomains, which contain 2–3 wt% of Al, occur within a single crystal of magnetite. The accumulation of NPs in the trace element-rich zones suggest that they form owing to supersaturation from a hydrothermal fluid, followed by entrapment during continuous growth of the magnetite surface. It is also concluded that mineral NPs promote exsolution of new phases from the mineral host, otherwise preserved as structurally bound trace elements. The presence of abundant mineral NPs in magnetite points to a complex incorporation of trace elements during growth, and provides a cautionary note on the interpretation of micron-scale chemical data of magnetite.

Keywords Magnetite · Nanoparticles · Zoning · Los Colorados

Introduction

Magnetite forms under a wide range of pressure and temperature conditions in igneous, metamorphic and sedimentary environments. Magnetite, $^{IV}Fe^{3+VI}(Fe^{2+}Fe^{3+})O_4$, $Fd3m$ and $Z = 8$, belongs to the spinel family described by general formula AB_2O_4. The presence of octahedrally and tetrahedrally coordinated positions in the magnetite structure allows for incorporation of cations via isovalent and

✉ Artur P. Deditius
  A.Deditius@murdoch.edu.au

1   School of Engineering and Information Technology, Murdoch University, Perth, WA 6150, Australia

2   Department of Geology, FCFM, University of Chile, Santiago, Chile

3   Andean Geothermal Center of Excellence (CEGA), FCFM, University of Chile, Santiago, Chile

4   Department of Earth Sciences, University of Michigan, Ann Arbor, MI, USA

5   Centre for Microscopy, Characterisation and Analysis (CMCA), The University of Western Australia, Perth, WA 6009, Australia

6   Bio21 Institute, University of Melbourne, Melbourne, VIC 3010, Australia

coupled substitutions at minor and trace concentrations. These include: Nb^{5+}, Ta^{5+}, Mo^{4+}, W^{4+}, Ti^{4+}, Si^{4+}, Ge^{4+}, Sn^{4+}, $V^{3+,4+}$, Cr^{3+}, Al^{3+}, As^{3+}, Ga^{3+}, Mn^{2+}, Zn^{2+}, Ni^{2+}, Co^{2+}, Cu^{2+}, Mg^{2+}, Ca^{2+}, and details about the mechanisms of incorporation have been recently reviewed by Dare et al. (2012) and Nadoll et al. (2014). Recent developments in laser ablation inductively coupled mass spectrometry (LA-ICP-MS) analyses of trace elements in magnetite have identified this mineral as an important petrogenetic indicator helping to identify the geological environment of ore formation (Dupuis and Beaudoin 2011; Dare et al. 2012, 2014, 2015; Nadoll et al. 2012, 2014; Boutroy et al. 2014; Neumann et al. 2017; Xie et al. 2017). For example, through a combination of trace element geochemistry, micro-textural relations, and Fe–O isotope pairs in magnetite, Knipping et al. (2015a, b) and Bilenker et al. (2016) proposed that some iron oxide–apatite (IOA) or Kiruna-type deposits may form by a mechanism that involves continuous growth of magnetite under purely igneous to magmatic-hydrothermal conditions.

While the variation of the chemical composition of magnetite at the microscale has received significant attention, there is still only a limited amount of information about the nanoscale behaviour of trace elements in magnetite (Newberry et al. 1982; Sitzman et al. 2000; Huberty et al. 2012; Xu et al. 2014). The nanoscale structural and magnetic properties of spinels are among of all mineral species, one of the most studied at the nanoscale (Harrison et al. 2002; Golla-Schindler et al. 2005; Papike et al. 2015; Colás et al. 2015; Haggarty 2016; Henderson et al. 2016). However, there is a dearth of data that constrain nanoscale behaviour of elements at trace and minor concentrations within the spinel group. The presence of impurities such as Al, Mg, Mn, V, and Cr, might lower the solvus temperature of spinels (von Grunewaldt et al. 1985), and higher concentrations of Mg and Al in magnetite may indicate disequilibrium during magnetite crystallization (Klemm et al. 1985). Titanium, on the other hand, is undoubtedly the most studied element in magnetite due to the presence of a complete solid solution between the endmembers magnetite and ulvöspinel (Price 1981; von Grunewaldt et al. 1985; Harrison et al. 2002; Bosi et al. 2009), although nanoscale heterogeneity has been observed. For example, magnetite domains of ~ 200 nm in size were reported in synthetic titanomagnetite (39% of Fe_2TiO_4) by Harrison et al. (2002). Silicon can be also relatively abundant in magnetite, leading to a series of studies attempting to resolve the structural details of its incorporation (Newberry et al. 1982; Huberty et al. 2012; Xu et al. 2014). Silicon is incorporated into magnetite in solid solution (Huberty et al. 2012) although it can form Si-bearing magnetite nanoprecipitates by exsolution from the host silician magnetite at low temperature (Xu et al. 2014). Golla-Schindler et al. (2005) reported compositional fluctuations in

the magnetite (Fe_3O_4)–hercynite ($FeAl_2O_4$) series produced experimentally at temperatures above 300 °C, which were interpreted as being caused by spinodal decomposition and compositional modulation at a wavelength of 16 nm. Furthermore, exsolution of Al–Mn–Fe-spinel nanoplates and formation of dislocations in magnetite from granulite facies rocks were attributed to the differences in Al concentration (Sitzman et al. 2000). These authors reported that the greater the concentration of Al in magnetite, the greater the extent of unmixing. Finally, multivalent vanadium species (V^{3+} and V^{4+}), have been proposed as an oxybarometer for geological systems containing spinel with V^{4+} being preferentially incorporated into inverse spinel (Rodgers et al. 1963; Papike et al. 2015). The use of V in magnetite as a monitor of fO_2 was further explored by Arato and Audetat (2016, 2017), who provided experimental calibration of a new oxybarometer for silicic magmas based on V partitioning between magnetite and silicate melt.

Among possible geological controls, temperature plays a major role on trace element incorporation into magnetite. Under high temperature, magmatic (igneous) conditions trace elements are either: (1) distributed homogeneously within the magnetite structure (Reguir et al. 2008); or (2) incorporated as melt inclusions (silicate or carbonatitic) or mineral particles including carbonates, apatite, phlogopite, biotite, chlorite, talc, minnesotaite, spinel, hercynite, monticellite, perovskite, cordierite, wolframite, pyrite, and chalcopyrite (e.g., Gaspar and Wyllie 1983; Sitzman et al. 2000; Guzmics et al. 2011; Hu et al. 2014a, b; Zhao and Zhou 2015). During cooling and/or as a result of changes in oxygen fugacity (fO_2), the incorporated (non-formula) trace elements tend to exsolve or separate from the magnetite matrix and form micron- to nano-sized inclusions of corundum, spinel, ilmenite, and ulvöspinel, which may be oriented along specific crystallographic directions in magnetite (Buddington and Lindsley 1964; von Grunewaldt et al. 1985; Dare et al. 2012; Hu et al. 2014a; Charlier et al. 2015). Analyses of some of these inclusion-rich magnetite grains using relatively large (a few to tens of microns) analytical spots that are typical of laser ablation inductively coupled plasma mass spectrometry (LA-ICP-MS), secondary ion mass spectrometry (SIMS) or even electron microprobe analyzer (EPMA) methods, can result in "averaging" the trace element content of magnetite. In fact, some studies have interpreted that these data represent the original chemical composition of magnetite before the exsolution of the secondary phases (Dare et al. 2012).

Despite these advances, no study documenting the nanomineralogy and nanochemistry of trace element-rich magnetite is currently available. Moreover, the relationship between nanotextural features such as oscillatory zoning and the occurrence of mineral NPs in magnetite is poorly understood. In fact, trace elements in magnetite crystallizing

under hydrothermal conditions tend to partition into growth or sector zones of variable thickness, sometimes as narrow as a few microns or less (e.g., Neumann et al. 2017). These trace element-rich zones have been interpreted as being sequentially precipitated either from hydrothermal fluids of variable composition, or more importantly of different origin (Dare et al. 2014, 2015; Knipping et al. 2015b). Therefore, obtaining high-resolution mineralogical information of these growth zones is crucial for interpreting the processes responsible for trace element partitioning in magnetite. Furthermore, and considering that the trace element and isotopic composition of magnetite is measured using EPMA, LA-ICP-MS or SIMS, high-resolution mineralogical data are relevant to identify factors that can bias the interpretation of micro-analytical data; i.e., the presence of sub-micron sized inclusions. Even for an analytical spot size of ~ 1 μm, which is typical for EPMA techniques, the excitation volume of a few cubic microns does not allow resolving the composition of individual nanoscale inclusions in magnetite, resulting in an average composition (NPs + matrix). Such nanoscale structural and chemical details can, however, be detected by using transmission electron microscopy (TEM) techniques (Utsunomiya and Ewing 2003; Ciobanu et al. 2011).

In this study, we present EPMA spot analyses and wavelength dispersive spectrometry (WDS) elemental maps of hydrothermal magnetite from the Los Colorados iron oxide–apatite (IOA) deposit in northern Chile. These magnetites are characterized by chemically distinct bands that repeat at regular distance in oscillatory zoning that mark abrupt changes in composition. Cross-sectional samples through the oscillatory zones were prepared by using focused ion beam (FIB), and samples were inspected using a combination of transmission electron microscopy (TEM) techniques including high-resolution imaging (HRTEM), selected area electron diffraction (SAED), high-angle annular dark-field scanning TEM (HAADF-STEM) and energy dispersive X-ray spectrometry (EDS). The TEM techniques helped to obtain structural and chemical information of both the magnetite matrix and the incorporated mineral nanoparticles. Our results revealed complex patterns of trace element incorporation into magnetite during growth, providing key evidence for the interpretation of deposit-scale mineralization events, which are often only apparent at the micro- to nano-scales.

Samples and methods

Magnetite samples were collected from the Los Colorados iron oxide–apatite (IOA) deposit, in the Chilean Iron Belt, which hosts more than 40 IOA deposits in the Coastal Range of northern Chile. All the deposits occur within the southern segment of the Atacama Fault System. The Los Colorados

deposit contains 70 M tonnes Fe in two parallel, magnetite-rich (> 90 modal %) tabular orebodies or "dykes" that measure 1500 m along strike, 150 m wide, and ~ 500 m deep. The West dyke contains ~ 63% total iron and the East dyke ~ 55% total iron. The dykes are bounded on the west by a fault and to the east by a brecciated zone that contains ~ 25% total Fe. Los Colorados is Cretaceous in age, and hosted in igneous rocks of the Punta del Cobre Formation (Fig. 1) (Knipping et al. 2015a, b; Reich et al. 2016).

The Los Colorados deposit offers a unique opportunity to investigate the nanoscale features of hydrothermal magnetite because: (1) the deposit lacks sodic/potassic alteration and supergene oxidation that overprints the main magnetite forming events and may obscure the primary geochemical signals; and (2) three generations of magnetite have been previously identified, from purely magmatic (igneous) to early and late hydrothermal (Knipping et al. 2015a, b). In particular, we focus here on the late hydrothermal magnetite in the brecciated/stockwork zone. Magnetite from this zone is trace element-rich, contains abundant micro- to nano-sized inclusions, and is characterized by oscillatory and sector zoning features, as reported by Knipping et al. (2015b). The mineral assemblage consists dominantly of magnetite and actinolite, with only minor apatite.

Compositional analyses were acquired using a JEOL JXA8530F electron microprobe equipped with five tunable wavelength dispersive spectrometers. Operating conditions were 40° take-off angle and a beam energy of 20 keV. The beam current was 50 nA, and the beam was fully focussed operating in point mode. Elements were acquired using analysing crystals LiF for Fe Kα, Cr Kα, Ni Kα, LiFH for V Kα, Mn Kα, PETJ for K Kα, Ti Kα, Ca Kα, and TAP for Si Kα, Al Kα, Na Kα, Mg Kα. The standards employed for instrument calibration were a selection of commercially available metals as well as synthetic and natural oxides and silicate minerals. The counting time was 20 s for Fe Kα, 30 s for K Kα, Na Kα, and 60 s for Mg Kα, Ti Kα, Ca Kα, Al Kα, Si Kα, Cr Kα, Ni Kα, V Kα, Mn Kα. The intensity data were corrected for time-dependent intensity (TDI) loss (or gain) using a self-calibrated correction for Si Kα, Na Kα, K Kα, Ni Kα, Mn Kα. Mean atomic number (MAN) background correction was used throughout. The background intensity data were calibrated and continuum absorption corrected for Si Kα, Al Kα, Na Kα, Mg Kα, Ti Kα, Ca Kα, K Kα, Fe Kα, Cr Kα, Ni Kα, V Kα, Mn Kα (Donovan and Tingle 1996; Donovan et al. 2016). Unknown and standard intensities were corrected for deadtime. Interference corrections were applied to Fe for interference by Mn, and to Cr for interference by V, and to V for interference by Ti, and to Mn for interference by Cr (Donovan et al. 1993). Detection limits ranged from 0.003 weight percent for Ca Kα and Si Kα to 0.004 weight percent for Mn Kα to 0.005 weight percent for Cr Kα to 0.017 weight percent for Na Kα. Oxygen
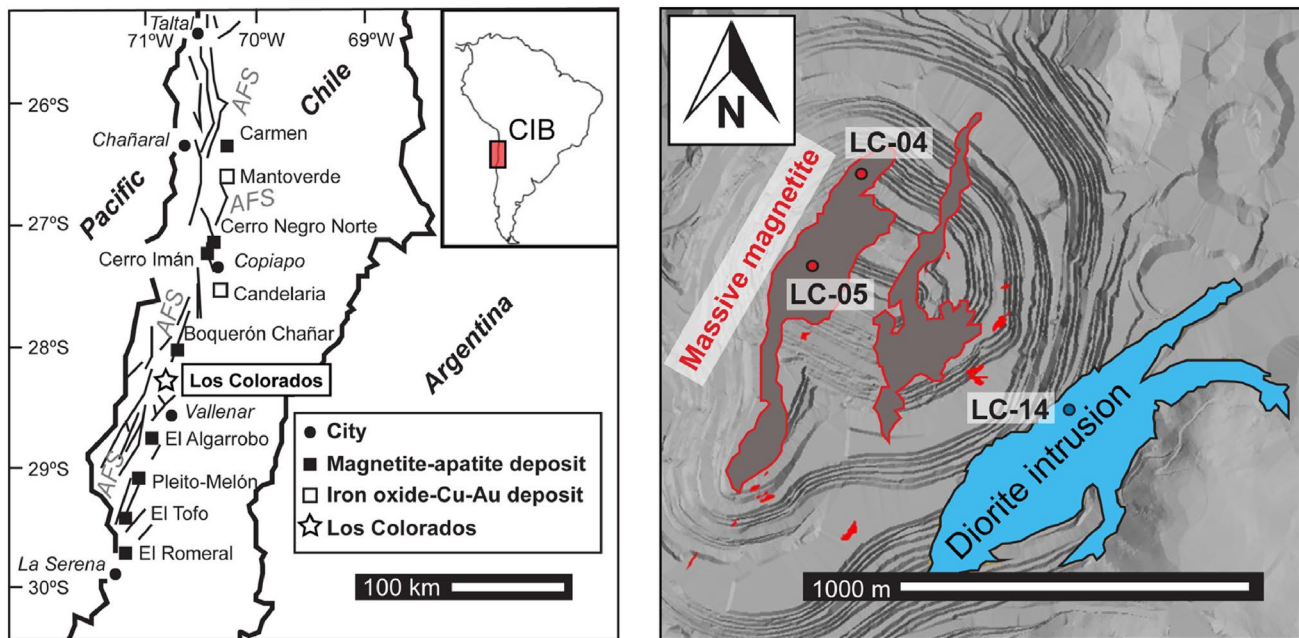
Fig. 1 Location of the Los Colorados IOA deposit (left) and map showing the two massive magnetite tabular orebodies and the diorite intrusion (right). The studied magnetite was retrieved from drill core LC-14 (167 m) that crosscuts the brecciated/stockwork zone between the eastern tabular body and the diorite intrusion. Magnetite from drill cores LC-04 and LC-05 was studied by Knipping et al. (2015a, b)

was calculated by cation stoichiometry and included in the matrix correction. The ZAF algorithm utilized was Armstrong/Love Scott (Armstrong 1988).

The thin-foil samples were prepared by using a FEI Helios NanoLab G3 CX DualBeam FIB at the Centre for Microscopy, Characterisation and Analysis (CMCA), The University of Western Australia, and a FEI Nova DualBeam FIB at the University of Melbourne. Sections prepared using the Helios G3 were extracted from the sample surface by in situ lift-out, welded onto a copper grid, thinned to electron transparency with a 30-kV ion beam where the beam current was progressively reduced from 2.5 to 0.23 nA, and then finally polished with a 5-kV beam with a 41-pA current. Subsequently, the samples were analysed at the CMCA using a Titan G2 80-2090 TEM/STEM with ChemiSTEM technology at 200 kV.

Results

Chemical composition of magnetite

Hydrothermal magnetite at Los Colorados occurs in 3–5 mm thick aggregates of zoned grains, with individual crystals varying in size from a few micrometres to a few millimetres across. Magnetite is spatially associated with actinolite (Fig. 2) and apatite. Based on the textural observations, the hydrothermal magnetite crystals are divided into three textural types referred to as magnetite-(X), magnetite-(Y) and magnetite-(Z). We highlight that these textural types are not to be confused with magnetite Types I, II, and III, which were defined by Knipping et al. (2015a, b) based strictly on chemical variability. The current study focuses exclusively on the late hydrothermal magnetite at Los Colorados, i.e., magnetite Type III after Knipping et al. (2015a, b).

Magnetite-(X) is euhedral and characterized by oscillatory and sector zoning, with darker shades of grey on the back-scattered electron (BSE) images that indicate enrichment in trace elements (Fig. 2a). Magnetite-(X) is partly recrystallized to fine-grained microcrystalline aggregates of magnetite-(X) and silicates (Fig. 2a, b). The fine-grained magnetite, ~ 5 μm in size, is porous and intimately intergrown with dominating amphibole (actinolite), which prevents acquisition of representative and accurate EPMA analyses. Magnetite-(Y) exhibits a tooth-like texture with grains ~ 500 μm in size, and trace elements have accumulated in sector zones (Fig. 2b). The third textural type is coarser-grained magnetite-(Z) that volumetrically dominates the three textural types of late hydrothermal magnetite described here. Magnetite-(Z) is characterized by oscillatory zoning, i.e., alternating trace element-rich and trace element-poor bands. The thickness of the individual bands in magnetite-(Z) varies between 2 and 10 μm (Fig. 2c–f).

The EPMA analyses reveal similar chemical compositions for magnetite-(X), -(Y) and -(Z). The major compositional variations occur between the trace element-rich and trace element-poor areas of magnetite (Figs. 2, 3; Table 1S; Supplementary Material). The concentrations of minor elements and trace element in magnetite-(X)–(Z) vary over relatively wide ranges (i.e., in wt%): SiO_2, from below detection limit (bdl) to 4.65 wt%; Al_2O_3, from 0.25 to 2.30 wt%; CaO, from bdl to 1.27 wt%; MgO, from 0.02 to 3.20 wt%; TiO_2, from 0.09 to 0.36 wt%; MnO, from 0.04 to 0.2 wt%; Na_2O, from bdl to 0.40 wt%; and K_2O, from bdl to 0.36 wt%. Six analyses of magnetite show elevated concentrations of TiO_2 (0.5–9.2 wt%) and MnO (0.4–6.6 wt%) indicating presence of ilmenite inclusions. The variable concentrations of these elements in magnetite suggest the presence of mineral nanoparticles (NPs) that are "invisible" to SEM and EPMA methods. These individual nanoparticles or clusters of particles account for an additional signal from the excitation volume generated by the electron beam. Unlike the previous elements, the concentration of V in magnetite is remarkably homogenous. V_2O_3 concentrations in magnetite-(X) and -(Y) vary from 0.38 to 0.40 wt%, whereas V_2O_3 in magnetite-(Z) is slightly lower, 0.31–0.36 wt%. The concentrations of NiO and Cr_2O_3, on the other hand, were below detection limit (Table 1S).

Positive correlations ($R^2 \geq 0.6$) are exhibited among Si, Al, Ca, Mg, K, and Na in magnetite (Table 1). However, these correlations should be treated with caution due to the possible impact of mineral NPs on the overall measured concentrations (See Discussion). Vanadium and Mn do not correlate with any of the other trace elements. Titanium positively correlates with Al ($R^2 = 0.6$) (Fig. 2; Table 1). These correlations are consistent with the spiky EPMA traverses that cut through the oscillatory zoning, where Si, Al, Mg, Ca, K and Na occur within the same bands (Fig. 2e, f). In contrast, the V profile is flat and does not correlate with any of the analysed trace elements (Fig. 2f). There is a weak positive correspondence between Ti and Mn, and most areas that are enriched with trace elements are typically depleted in Fe (Fig. 2e, f).

The EPMA elemental mapping of magnetite-(X), -(Y), and -(Z) revealed a consistent distribution of Al, Si, Mg, and Ca between the trace element-rich (median values: 1.17, 1.49, 0.63, and 0.36, respectively; in wt% oxides) and -poor (median values: 0.51, 0.17, 0.13, and 0.05, respectively; in wt% oxides) zones. Trace elements tend to accumulate in growth and sector zones in magnetite-(X), whereas magnetite-(Y) hosts numerous particles (Fig. 3). Silicon and Al form particles in the trace element-rich zones of magnetite-(Z), whereas no particles were detected on the Ca and Mg elemental maps of magnetite-(Z) (Fig. 2d). The distribution of Ti is complex, and in magnetite-(Z) in particular, Ti shows a marked oscillatory zoning (Fig. 2d). Titanium forms Ti-rich particles (together with Mn) in the trace element-poor bands (zones depleted in Al, Mg, Si, and Ca), but it is homogeneously distributed in some of the trace element-rich bands. Titanium is typically below detection limit within the zones separating trace element-rich and trace element-poor bands (Fig. 2d). Due to its complexity, high-resolution analyses using TEM were focused on the oscillatory-zoned hydrothermal magnetite [magnetite-(Z)].

Structure, zoning and nanoparticles

Microscopic examination of magnetite-(Z) reveals no evidence of dissolution or reprecipitation processes, which could change the distribution of trace elements and thus make inaccessible its original geochemical signal. The characteristic features of dissolution–reprecipitation textures are irregular grain boundaries between different generations of minerals, corrosion rinds, and porosity (e.g., Putnis 2009). The HAADF-STEM images and EDS reveal the presence of elemental zoning, Al-rich domains and numerous NPs in the magnetite-(Z) matrix (Figs. 4, 5, 6, 7). The EDS elemental mapping across the oscillatory zoning in magnetite-(Z) showed relatively higher amounts of trace elements in the zones hosting NPs than in the trace element-poor zones (Figs. 4, 5, 6, 7); the concentrations of trace elements exhibited a negative correspondence with Fe (Fig. 4). The concentrations of trace elements such as Si, Ti, Al, V, Mg and Ca in the magnetite matrix hosting mineral NPs (trace element-rich zones) reaches 0.3, 0.2, 0.6, 0.3, 0.4 and 0.2 wt%, respectively (Table 2). The HRTEM images and Fast Fourier Transform (FFT) analyses do not show signs of structural distortion between the alternating trace element-poor and trace element-rich zones. The structural analysis point to a single crystal of magnetite-(Z) (Fig. 4b, c), which suggests continuous growth of magnetite during formation of the oscillatory zoning. The trace elements in the matrix of the enriched zones are distributed homogeneously, with the exception of Al (Figs. 4d–g, 5). Bright-field TEM images revealed the presence of Al-rich, elongated "darker" areas (up to 40×4 nm in size) within a single crystal of magnetite-(Z) (Fig. 5a–d). No other trace elements correlate with the Al distribution (Fig. 5—elemental maps). High-resolution images and FFT analyses show irregular contrast and discoidal diffraction maxima suggesting defect accumulation and possible formation of anti-phase boundaries (Fig. 5c). The concentration of Al in the Al-rich regions of the magnetite-(Z) matrix is 2.3–2.5 wt%; (EDS analyses). However, Al tends to concentrate at the grain boundaries between NPs and the magnetite matrix where its concentration increases to 17 wt%. This concentration translates to ~60 mol% of hercynite, $FeAl_2O_4$ (Fig. 5).

The structural observations coupled with the qualitative TEM-EDS elemental maps and point analyses (Table 2)
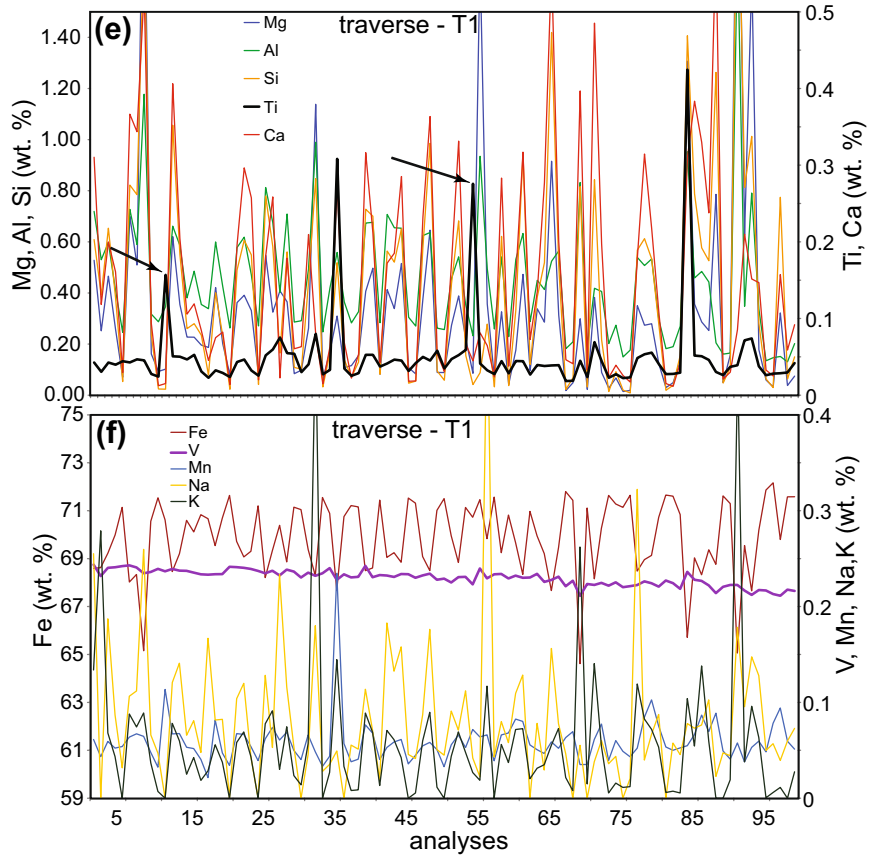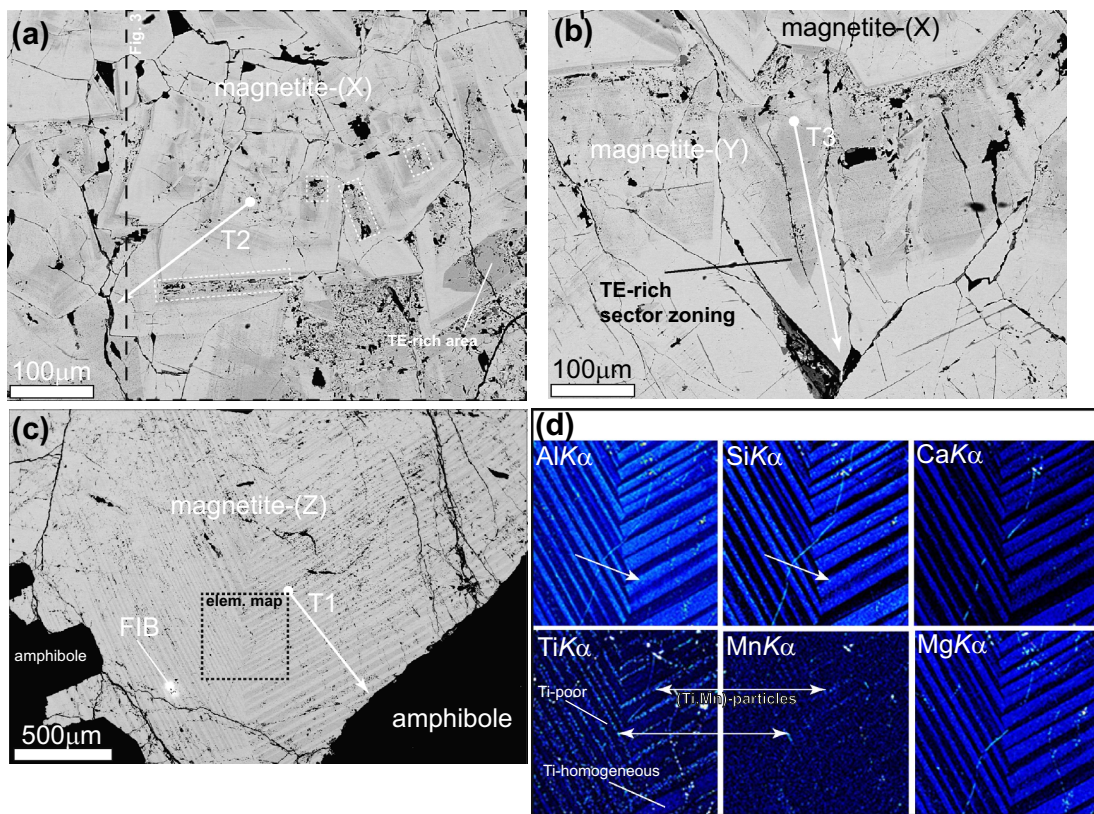
◄**Fig. 2 a–c** BSE images of the three different textural types of magnetite (X, Y, and Z). WDS X-ray maps for selected elements are shown in **d** and EMPA traverses showing changes in element concentrations (in wt%) are shown in **e, f**. The white arrows mark the positions of the traverses (dot—the beginning, arrowhead—the end; see supporting information for the analyses). **d** Elemental mapping of Al, Si, Ca, Ti, Mn and Mg. Note: (1) a similar distribution of Al, Si, Ca, and Mg between alternate trace elements-rich and -poor zones; (2) the presence of (Si, Al)-particles in trace element-rich zones (white arrows); (3) a partitioning of Ti between particle-rich zones, homogeneously distributed Ti in Ti-rich zones, and Ti-poor zones; (4) a coherent correlation between Ti and Mn zones hosting particles (white arrows with double arrowhead); (5) concentration of Mg, Al, Si, Ti, Ca (in wt%) along traverse-T1; note a shift of the maximum concentrations of Ti in comparison with the local maxima for other trace elements (black arrows). **f** Concentration of Fe, V, Mn, Na, and K in (wt%) along traverse-T1. Note the relatively flat and slightly decreasing concentration of V towards the grain boundary between magnetite and actinolite and inverse correlation between Fe and Mg, Al, Si, Ca, Na, K, Ti and Mn. The white dotted squares mark the areas of fine-grained magnetite-(Y)

revealed the presence of six types of crystalline NPs: diopside, enstatite, amphibole (tremolite–actinolite), mica (phlogopite) and (Fe–Ti)-oxides identified as ulvöspinel and Ti-rich magnetite. As revealed by SAED and FFT patterns, all NPs are hosted within a single crystal of magnetite (Fig. 5b, c), and no porosity associated with NPs and/or in the magnetite-(Z) matrix was identified during TEM observations. Euhedral diopside NPs, up to 400×100 nm in size occur as chemically homogeneous single crystals (Fig. 7). Diopside NPs are separated from other nanophases present in the magnetite-(Z) matrix. Diopside, enstatite and Fe–Ti oxide NPs are misoriented with respect to the magnetite structure. The low-magnification TEM images of anhedral enstatite NPs, up to ~ 100 nm in size, revealed the presence of a modulated texture (Fig. 7a, c, d). The thickness of the individual domains/lamellae varies between 2 and 5 nm, and the boundary between the individual lamellae is diffuse (Fig. 7d). The FFT analysis of the HRTEM image suggest that the lamellae consist of clinoenstatite that form twinning on (100) planes (Fig. 7d). However, the EDS elemental mapping of the enstatite particles did not detect fluctuations in the chemical composition of the NPs, which if present would suggest a spinodal decomposition or exsolution (Weinbruch et al. 2003). Unfortunately, no reliable EDS analysis of enstatite was obtained due to the difficulty of collecting a pure spectral analysis of the small enstatite particles without some residual Fe signal from the surrounding magnetite-(Z) matrix. Amphibole NPs form elongated euhedral single crystals, 500×50 nm in size (Figs. 4, 5; 7g, h). The HRTEM observations revealed that amphibole NPs are beam-sensitive, with an increasing fraction of amorphous material forming due to exposure to the electron beam (Fig. 7g, h). The EDS analyses of amphibole NPs show Mg and Si as the two main cations and smaller amounts of Na and Fe

(Table 2). A rare mica, probably phlogopite, was found in mineral aggregates with amphiboles and Fe–Ti oxides. It has a planar morphology and typical length > 200 nm and width of 20–40 nm (Fig. 6). The diffraction pattern indicates the (001) basal plane to have a spacing of ~ 0.98 nm. The streaks observed on the diffraction pattern between the main diffraction maxima of phlogopite indicate stacking disorder (Fig. 6c) (Dobrzhinetskaya et al. 2009). Ulvöspinel and Ti-rich magnetite NPs form single crystals and have a variable size from 20 to 100 nm (Figs. 4, 5, 6; Table 2). Vanadium is remarkably absent in the trace element-bearing NPs, including Ti-rich NPs, and is homogeneously distributed in the trace element-rich zones in magnetite (Fig. 5).

Discussion

Geochemistry of hydrothermal magnetite

The trace element geochemistry of magnetite and its genetic interpretation have been extensively explored, and compositional differences have been used in recent studies to construct discriminant diagrams that differentiate various styles of mineralization (e.g., Dupuis and Beaudoin 2011; Dare et al. 2012, 2014; Nadoll et al. 2014). Analyses of the late hydrothermal magnetite-(X), -(Y), and -(Z) from the Los Colorados IOA deposit, reported in this study, plot in the field of porphyry and skarn deposits confirming the involvement of a magmatic-hydrothermal aqueous fluid, as previously suggested by Knipping et al. (2015b) (Fig. 8a). In addition, the analyses cluster along a descending temperature trend that suggests crystallization from an evolving fluid under high-temperature conditions > 300–500 °C (Fig. 8b) (Nadoll et al. 2014; Knipping et al. 2015b).

Considering a continuum from purely magmatic to late hydrothermal conditions, data show that hydrothermal magnetite at Los Colorados was progressively depleted in (Mn + Mg) and enriched with (Si + Al) (Fig. 9). This increase in the Si and Al concentrations shows that the composition of oscillatory-zoned hydrothermal magnetite-(Z), studied here (Fig. 2), is highly consistent with an origin related to the latest stages of (breccia/stockwork-like) mineralization characterized by higher fluid/rock ratio (Hu et al. 2014b), in comparison to the primary magmatic-hydrothermal magnetite present in the tabular orebodies or "dykes".

A significant fraction of the analysed magnetite in this study carries a geochemical signature similar to magnetite from skarn deposits, in particular the trace element-rich zones of magnetite-(Z) (Fig. 8a). Such a large compositional variability, even within a single crystal, exemplifies the complexities in using magnetite discriminating diagrams to elucidate the origin of the deposit. Notwithstanding these difficulties, our nanoscale observations complement the
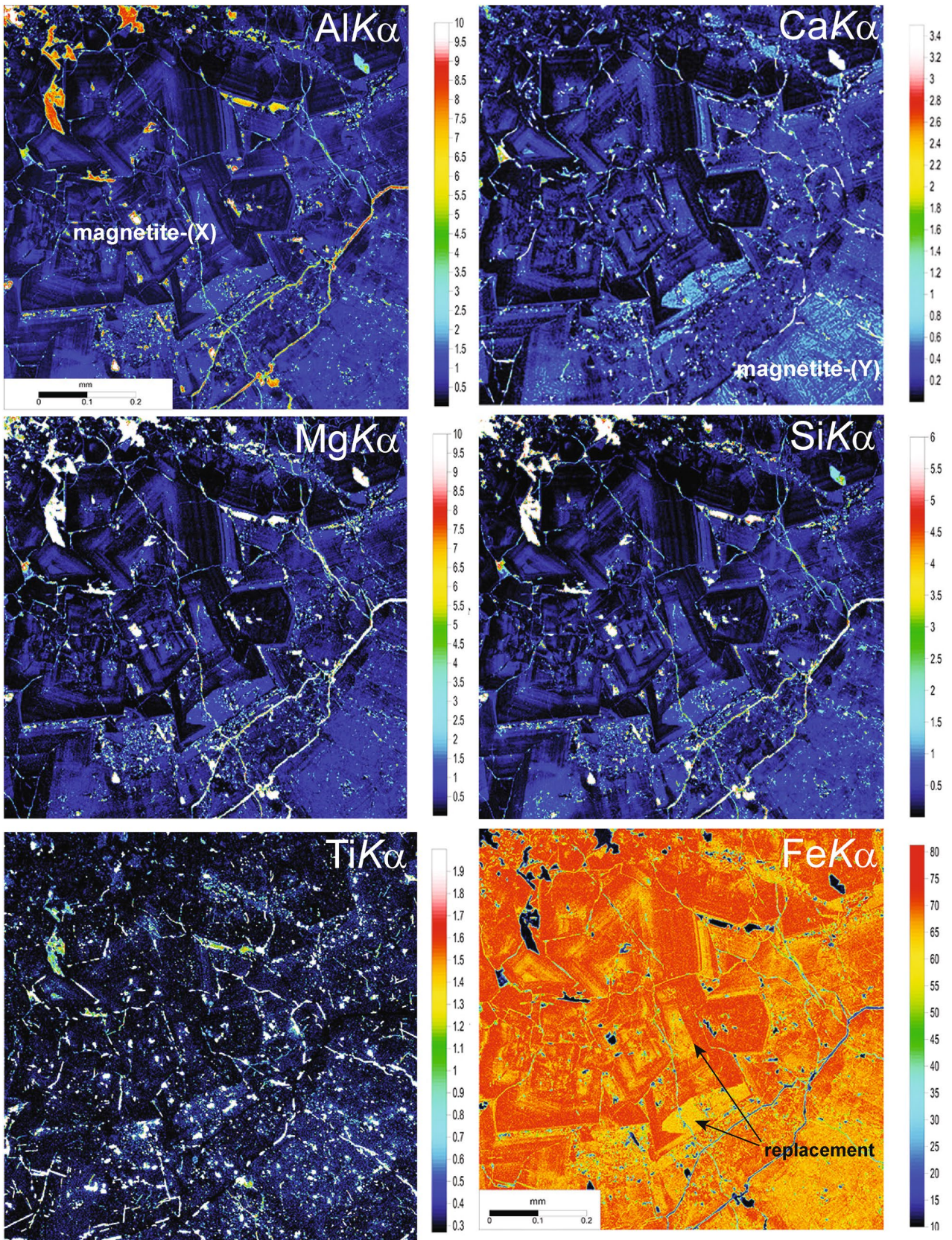
◀**Fig. 3** WDS X-ray elemental maps of the magnetite-(X) and -(Y); note the coherent relative increase in the amount of Al, Ca, Mg and Si in the trace element-rich zones that inversely correlates with Fe; the distribution of Ti is dominated by particles with some Ti accumulated in the growth zones

chemical information shown in Fig. 8a, and are consistent with skarn-type mineralogy, i.e., diopside NPs (Fig. 7a, b). The occurrence of diopside and magnetite is widely reported in Fe skarn deposits (e.g., Hu et al. 2014b; Yang et al. 2017), and fluid inclusion data in diopside indicate homogenization temperatures of ~ 448–598 °C (Yang et al. 2017), similar to the inferred temperatures for Los Colorados magnetite-(Z) based on magnetite composition. The possible presence of diopside during early stages of hydrothermal ore formation at Los Colorados is well aligned with the reported Mg-rich clinopyroxene compositions (Knipping et al. 2015b). The presence of amphibole NPs in magnetite (Fig. 7c, d) is also similar with mineral occurrences in skarn deposits.

Oscillatory zoning in hydrothermal magnetite

Changes in the chemical composition of oscillatory bands in silicates, oxides, sulphides and phosphates may reflect the crystallization from fluids of fluctuating elemental composition (Shore and Fowler 1996; Deditius et al. 2009; Tardani et al. 2017). At Los Colorados, it is noteworthy that a marked oscillatory zoning was only preserved in magnetite-(Z) (Fig. 2). In contrast, the corrosion rinds and truncated zoning in euhedral crystals of hydrothermal magnetite-(X) (Figs. 2, 3) document that dissolution and reprecipitation processes (Putnis 2009) played a significant role regulating the trace element geochemistry. Such textures have been interpreted as evidence of compositional re-equilibration of magnetite in Fe skarn deposits (Hu et al. 2014a, b) and Kiruna-type deposits (Heidarian et al. 2016). However, the reequilibration of magnetite-(X) did not affect its trace element signature, i.e., the analyses of all generations of magnetite plot as a single cluster on the Al + Mn vs. Ti + V diagram (Fig. 8). Therefore, the observed features indicate that magnetite-(X) formed from a hydrothermal fluid of a relatively stable composition, and the zoning reflects depletion or increase in the content of trace elements near the surface of the growing magnetite.

Trace elements in magnetite-(Y) tend to partition into the sector zones (Fig. 2b), which suggests that crystal growth involved the symmetrically non-equivalent faces and/or surface related size control over the incorporated ions (Watson and Liang 1995; Stowell et al. 2011). However, some equilibrium between advancing surfaces of the magnetite crystals and the fluid has to be maintained to preserve this type of texture (Watson and Liang 1995). The sector zoning in magnetite-(Y) suggests that it was precipitated under

local equilibrium conditions with selective partitioning of trace elements and crystal growth rates exceeding the lattice diffusion rates (Watson and Liang 1995; Shtuckenberg et al. 2009; Stowell et al. 2011). The change in the mechanisms of trace element incorporation from sector zoning of magnetite-(Y) to oscillatory zoning of magnetite-(Z) reflects the transition from the selective adsorption of the trace elements to kinetic attachment during rapid non-equilibrium growth of the magnetite crystals. This phenomenon most likely resulted from rapid depletion and subsequent increase in Si, Ti, Al, Mg, Mn, Ca and Na in the hydrothermal solution (e.g., Putnis et al. 1992; Shore and Fowler 1996; Stowell et al. 2011). The sharp compositional boundaries between the alternate trace element-rich and -poor zones in magnetite-(Z) within single crystals of magnetite imply preservation of the original oscillatory zoning (Figs. 2c, d, 4), which requires the growth rate of the crystal to be higher than intracrystalline diffusion (Watson and Liang 1995). The presence of mineral NPs in the trace element-rich zones (particularly the multi-mineral aggregates), and its absence in the trace element-poor zones, suggests that the hydrothermal fluid became supersaturated with respect to silicates and oxides (Figs. 5, 6, 7). The aggregates of mineral NPs or trace element-rich fluid inclusions were trapped during progressive growth of the magnetite-(Z) surface (Watson and Liang 1995; Watson 1996, 2004; Stowell et al. 2011). The compositional oscillation in magnetite-(Z) from Los Colorados involves all elements except V, which suggests that the trace element distribution was controlled by changes in the composition of the magmatic-hydrothermal fluid and the crystal-chemical properties of magnetite, rather than fluctuations of fO_2.

Mechanisms of trace element incorporation into magnetite growth zones

Aluminium, Si, Mg, Mn, Ca, and Na partition into the same trace element-rich growth zones in magnetite-(Z). This coexistence suggests compositional availability in the hydrothermal fluid. However, the distribution of Ti only partially coincides with these trace element-rich zones (Fig. 2d–f). This difference in the behaviour of Ti may be related to: (1) compatibility of Ti with magnetite structure; (2) the changes in the diffusivity of Ti^{4+} in the near-surface environment during magnetite growth comparing with the other elements (Kouchi et al. 1983); and (3) mobility and/or different source/s of Ti. Adsorption of the trace elements on the crystal surface of the growing magnetite may be one of the most important mechanisms for the formation of the oscillatory micro- and nano-zoning. This may result in the inhibition of the crystal growth, particularly under lower temperature conditions (Davis et al. 2000). However, the relatively high temperatures of crystallization for hydrothermal magnetite

Table 1 Correlations between the trace elements in magnetite (the data representing inclusions have been removed from the calculations)

| X	Si	Ti	Al	V	Ca	Mg	Mn	K	Na	Fe(II)	Fe(III)
Si	**X**										
Ti	**0.61**	**X**									
Al	**0.83**	**0.60**	**X**								
V	0.00	0.00	0.00	**X**							
Ca	**0.85**	0.38	0.54	0.00	**X**						
Mg	**0.87**	0.46	**0.68**	0.00	**0.76**	**X**					
Mn	0.00	0.11	0.00	0.00	0.00	0.00	**X**				
K	**0.76**	0.59	**0.80**	0.05	0.50	0.56	0.00	**X**			
Na	0.53	0.41	**0.61**	0.00	0.36	0.57	0.00	0.56	**X**		
Fe(II)	**0.89**	0.16	**0.77**	0.00	**0.73**	**0.79**	0.04	0.33	0.25	**X**	
Fe(III)	**0.89**	0.16	**0.77**	0.00	**0.73**	**0.79**	0.04	0.33	0.25	**1.00**	**X**

Higher values are in bold

at Los Colorados (minimum 300 °C as inferred from Fig. 8a) most likely prevented the adsorbed species from acting as inhibitors of the crystal growth.

Magnesium, Mn and Al fit best into the magnetite structure whereas Na, Ca, and Si are highly incompatible and their ionic radii lie out of the "optimum radius" of $\pm$ 15–18% radius variation (Goldschmidt 1954; Dare et al. 2012). A detailed discussion of Al incorporation is provided in the following section. The incorporation of Mg and Mn into magnetite depends on the ionic radius, site occupancies and the composition of the fluid phase (Toplis and Corgne 2002). The TEM observations (Figs. 5, 6) and EDS analyses of trace element-rich zones document 0.4 wt% of Mg in solid solution (Table 2), when EPMA analyses indicate as much as 3.2 wt% of MgO. Similarly, it was reported that elevated concentrations of Na and Ca in magnetite suggest the presence of mineral NPs (Nadoll et al. 2014). Indeed, the measured concentration of Ca in the matrix of magnetite does not exceed 0.2 wt% (Table 2). However, in the investigated samples some Na also occurs as a structurally bound element in magnetite-(Z) (Figs. 6, 7; supplementary materials). Furthermore, silicon is one of the most abundant elements in the analysed magnetite and occurs as mineral NPs and in solid solution (up to 0.3 wt%), in agreement with previous observations by Newberry et al. (1982). For example, Xu et al. (2014) identified the γ-Fe$_{1.5}$SiO$_4$ phase in Si-rich magnetite from a banded iron formation in Western Australia. However, this phase was not identified in magnetite-(Z). It is important to note that trace element enriched zones in magnetite also show highly deformed structural domains (Figs. 4c, 5b). Limited experimental data on partitioning of Cr, V and some divalent metals between magnetite and hydrothermal fluid indicate preferential partitioning of Cr and V into magnetite (Tauson et al. 2017) also reflected in data for burial metamorphic magnetite (Nadoll et al. 2017). Manganese tends to accumulate in ilmenite, identified in the studied material (Fig. 2d); while Zn, Cu, and Cd partitions

into fluid phase (Ilton and Eugster 1990). Under high-temperature, magmatic (silicic) conditions the divalent cations tend to partition into the titanomagnetite rather than to the associated melt with increasing fO$_2$ (Sievwright et al. 2017). Thus, it is likely that hydrothermal magnetite is capable of accommodating strain related to differences in the ionic size and charge during fast growth of the trace element-rich zones, possibly enhanced by the relatively high temperature conditions of magnetite formation at Los Colorados.

Otherwise remarkably constant, there is a relatively small decrease in V concentration from magnetite-(X) to -(Z) (Fig. 2; supplementary materials) (see also Knipping et al. 2015b). Incorporation of V into magnetite is controlled by its crystal-chemical properties and fO$_2$ of the hydrothermal fluid (Rodgers et al. 1963; Papike et al. 2015; Günther et al. 2017). Relatively constant V content in magnetite grains across zoning suggests limited variations in fO$_2$, which affects the V^{4+}/V^{3+} ratio during precipitation of magnetite and thus the incorporation of V into the structure. Both vanadium species are restricted to the octahedral sites of the magnetite structure (Papike et al. 2015). While coulsonite has a structure of "normal" spinel and is an endmember hosting V^{3+}, Fe^{2+}V^{3+}$_2$O$_4$, the V^{4+} endmember, ^{IV}Fe^{2+}^{VI}[Fe^{2+}V^{4+}]O$_4$, was not reported in natural samples (Rodgers et al. 1963). Magnetite is an inverse spinel that preferentially incorporates V^{4+} (Papike et al. 2015). Under higher-T and -P magmatic conditions of 800 °C and 0.5 GPa, V^{3+}/V^{4+} in binary Fe–V–O spinel solid solution is controlled by stoichiometry (Fe^{2+}/Fe^{3+}) and it is independent of fO$_2$ (Sossi et al. 2018). However, such conditions have limited application to the studied system and the presence of a significant fraction of V^{3+} in magnetite results in the exsolution of coulsonite domains (Wang et al. 1989). These exsolutions were not identified in the investigated samples, suggesting that V^{4+} is an important component of the magnetite structure. Another alternative explanation would involve re-equilibration of V zoning in the magnetite. However, if such re-equilibration
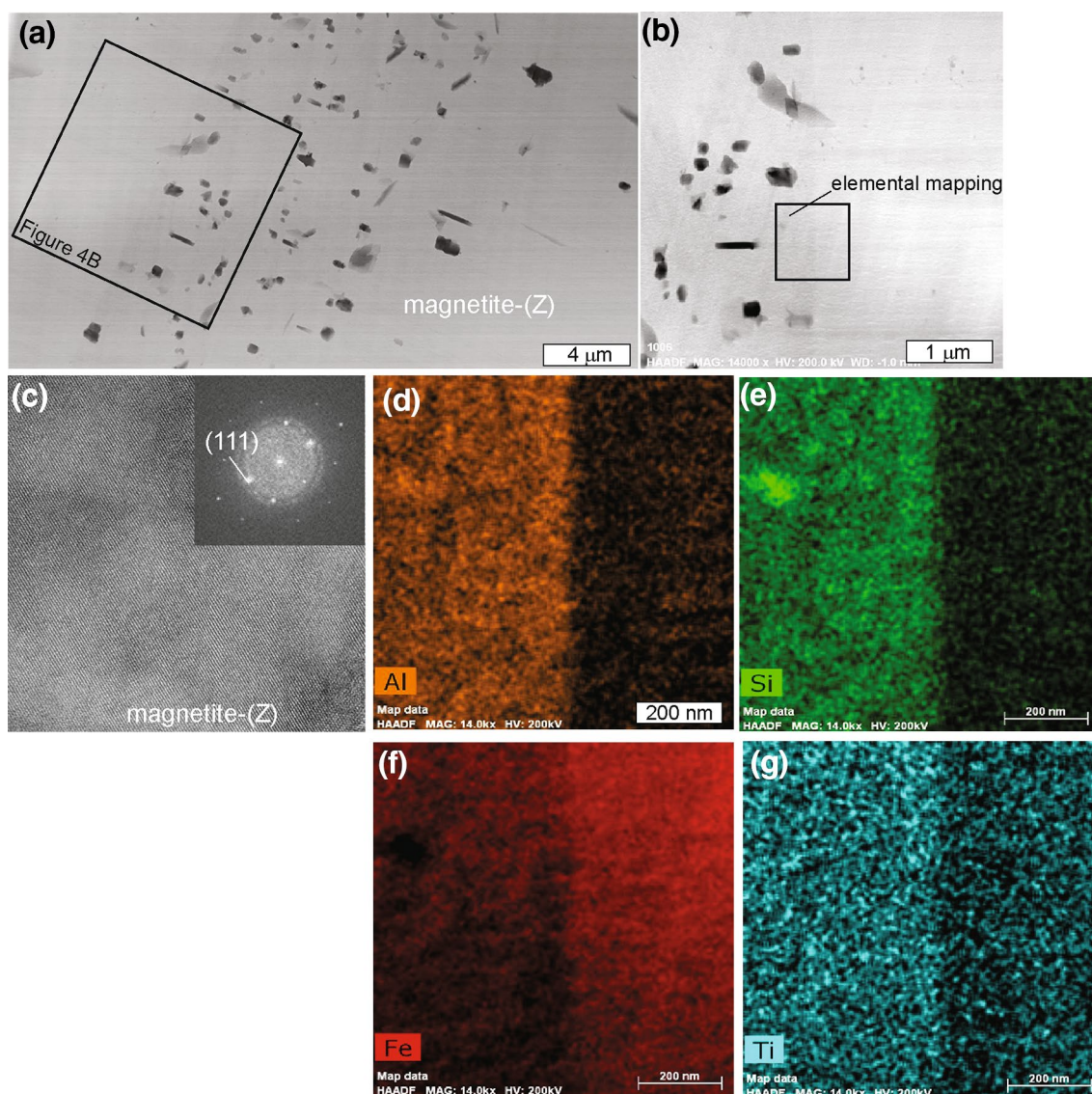
Fig. 4 a BSE and **b** HAADF-STEM images of the FIB section of magnetite cut at the boundary between particle-rich and particle-poor growth zones. **c** HRTEM image of magnetite single crystal, as deduced form the FFT pattern; image collected from the area that include both zones. **d**–**g** TEM-EDS elemental maps. Note the sharp change in the relative concentrations of Al, Si, Fe and Ti, between the zones, the homogeneous distribution of the trace elements within each zone, and the relatively enriched concentrations of trace elements (Al, Si, Ti) in particle-rich zones, which are inversely correlated with the amount of Fe (**f**)

occurred it would result in at least partial homogenization of the other elements accumulated in the oscillatory zones (Connoly and Burnett 2003). Therefore, and considering the presence of well-preserved oscillatory zoning, it is suggested that no diffusion and/or re-equilibration of V occurred in magnetite.

Mineralogy and formation of the NPs

All identified NPs are crystalline and are hosted by a single crystal of magnetite-(Z). The high-resolution structural observations and TEM-EDS analyses of the hydrothermal magnetite-(Z) revealed Al-rich domains and mineral NPs of diopside, enstatite, amphibole (tremolite–actynolite), mica (phlogopite), Ti-rich magnetite, and ulvöspinel. Single crystal magnetite hosts Al-rich nanodomains (Fig. 5b), and their stability is strongly dependent on temperature (Nadoll et al. 2014 and references therein). The presence of the Al-rich domains (Fig. 5) is consistent with the progressive incompatibility of Al in magnetite during cooling and structural ordering. Aluminium-rich nanodomains in the magnetite matrix have ~ 2–3 wt% of Al. However, the amount of Al increases at the grain boundaries between magnetite to 17 wt% of Al ($Hercynite_{62}Magnetite_{38}$). The other trace

Table 2 Chemical composition of nanoparticles and hosting magnetite by means of TEM-EDS (in wt%)

Elements	Mag ideal	Mag[a]	Mag[a]	Mag[a]	Usp ideal	Usp	Ti-Mag	Di ideal	Di	Di	Amp	Amp	Al (dom.-max.)
Fe	72.36	72.8	71.9	70.3	49.96	50.0	61.3	–	bdl	6.2	2.4	5.6	7.7
Ti	–	0.1	0.2	0.2	21.42	16.0	6.2	–	bdl	bdl	bdl	bdl	bdl
Si	–	0.3	0.3	0.2	–	bdl	0.5	25.94	26.1	23.1	13.3	17.0	12.3
Al	–	0.4	0.6	0.6	–	bdl	0.6	–	bdl	0.7	5.5	7.1	17.3
V	–	0.2	0.3	0.3	–	bdl	0.1	–	bdl	bdl	bdl	bdl	bdl
Ca	–	0.1	0.2	0.1	–	bdl	bdl	18.51	15.3	14.5	bdl	bdl	7.1
Mg	–	bdl	0.4	0.3	–	bdl	0.4	11.22	9.6	7.4	12.0	13.8	2.1
Mn	–	bdl	bdl	1.0	–	bdl	bdl	–	bdl	bdl	bdl	bdl	bdl
K	–	bdl	0.1	bdl	–	bdl	bdl	–	bdl	bdl	bdl	bdl	bdl
Na	–	bdl	bdl	bdl	–	bdl	bdl	–	bdl	bdl	2.2	2.8	bdl
O	27.64	26.1	25.4	26.6	28.63	34.0	30.9	44.33	48.9	47.5	64.73	53.8	53.4
H	–	–	–	–	–	–	–	–	–	–	–	–	–
Total	100	100.0	99.4	99.6	100.0	100.1	100.0	100.0	99.9	99.4	100.1	100.1	99.9

*Mag* magnetite, *Usp* ulvöspinel, *Di* diopside, *Amp* amphibole, *incl.* inclusion, *dom* domain

[a] Trace element-rich zones

elements identified in the magnetite do not partition into the Al-rich areas. The thickness of the Al-rich domains is within the range of a few nanometres (Fig. 5a), similar to the hercynite domains in synthetic samples that experienced spinodal exsolution of $Mag_{50}Hec_{50}$-$Mag_{30}Hec_{70}$ (Golla-Schindler et al. 2005). However, the HRTEM image does not show the characteristic "tweed" texture for spinodal decomposition in the magnetite–hercynite system (Golla-Schindler et al. 2005). Nanoparticulate, 40×1–3 nm Al–Mn–Fe-spinel precipitates were also found in magnetite, which experienced high-T metamorphism at 775 °C with the concentration of Al varying from 0.35 to 1.04 wt% (Sitzman et al. 2000), and points to the major role of Al as an element responsible for the formation of hercynite exsolution. The separation of the Al-rich domains in the magnetite structure (Fig. 5a) may be an effect of cation ordering in magnetite (inverse spinel) forming hercynite (normal spinel). This suggestion is supported by the orientation of the Al-domains parallel to the $\langle 111 \rangle$ orientation of magnetite (Fig. 4), similarly to the Al-rich platelets reported by Sitzman et al. (2000). These platelets were described as intermediate compositions between galaxite and hercynite. The relatively uniform distribution of Al-domains in the magnetite matrix suggests that they formed via homogeneous nucleation. The HRTEM observations revealed that the Al-rim is composed of randomly oriented NPs ~ 10 nm in size (Fig. 5c) and the diffraction pattern matches the one of hercynite. The presence of the Al-rim on silicate NPs suggests that Al, i.e., hercynite-rich domains, were preferentially formed at the interface between magnetite and the other NPs. The localized precipitation of hercynite might be a result of defect removal from the magnetite structure or a higher concentration of Al near the surface of the silicate NPs; and/or promotion of the formation

of hercynite domains via surface controlled exsolution during the magnetite growth. Thus, mineral NPs may promote exsolution of new phases from the mineral host. Magnetite containing higher concentrations of Al increases the level of unmixing of Al-spinels (Sitzman et al. 2000). No Al-rich rims were found on ulvöspinel or Ti-rich magnetite, which is consistent with the observation of Harrison et al. (2002), who found little or no Al (in addition to Mg and Ti) in the magnetite nanoblocks immersed in ulvöspinel. The observed separation of Al-rich domains from the magnetite structure is a result of limited solid solution between Al and Fe spinels, with the compositions of Al-richest domains falling into the miscibility gap for the magnetite–hercynite solid solution at the temperatures below 860 °C (Golla-Schindler et al. 2005). The presence of Al-domains signifies the importance of this element during phase separation from the magnetite structure.

Silicates and oxide NPs in late hydrothermal magnetite from Los Colorados occur as single particles (enstatite, amphibole, diopside) and/or form mineral aggregates (Ti–Fe oxides, phlogopite, diopside) (Figs. 4, 5, 6, 7). Clinoenstatite was not found in the matrix of the rock, which is not a unique phenomenon (Liu et al. 2014). However, the random orientation with respect to the magnetite structure, spherical shape and twinning of the clinoenstatite NPs, suggest that they formed at higher temperature, possibly under hydrothermal conditions, and were subsequently incorporated/trapped into the magnetite. The sharp boundaries between the twinned domains (Fig. 7d) suggest it is unlikely that they formed by unmixing or spinodal decomposition (Weinbruch et al. 2003).

Actinolite and/or clinopyroxene occur in polycrystalline inclusions, > 10 µm in size, in massive magnetite at Los
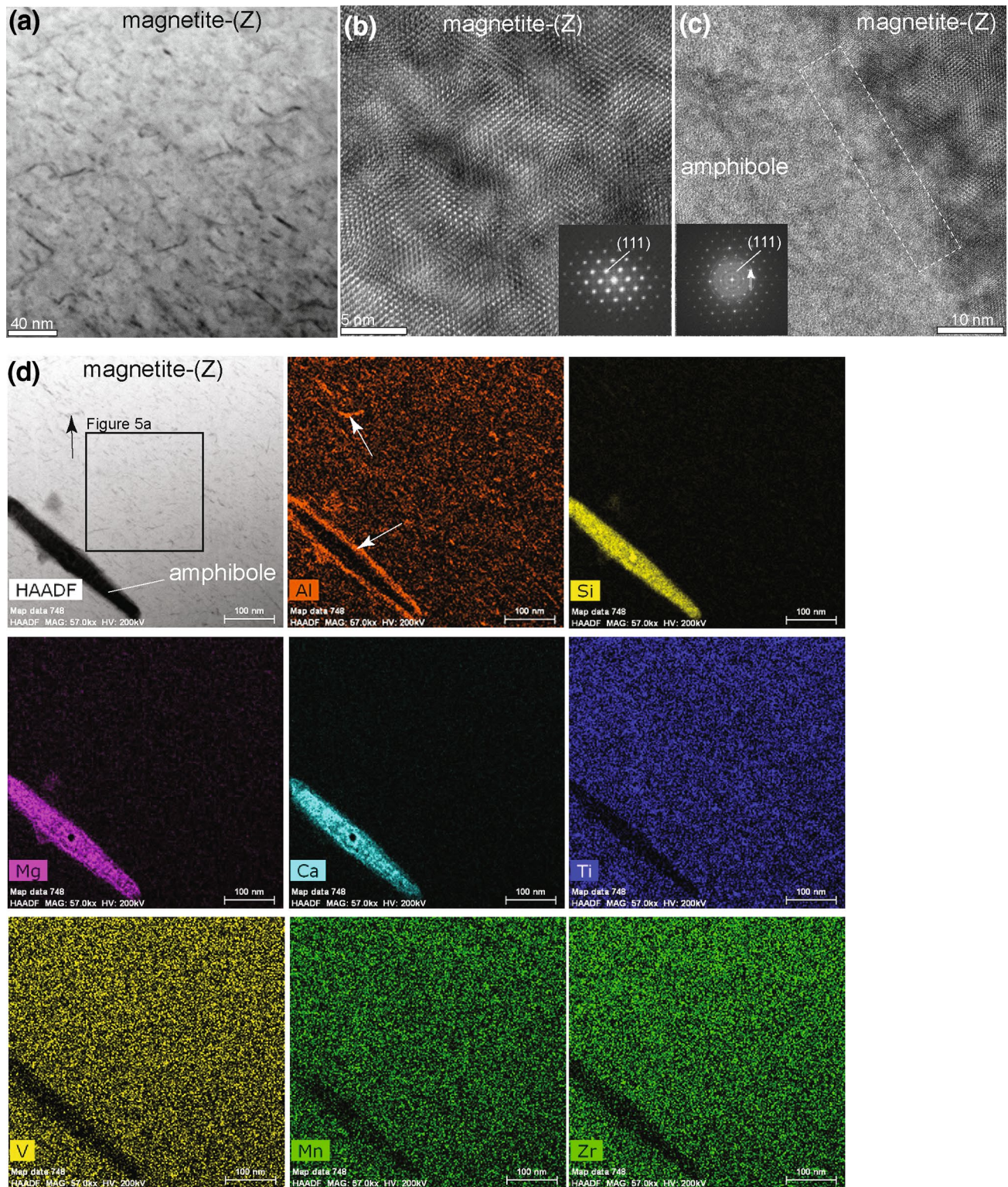
Fig. 5 **a** Bright-field TEM image of Al-rich domains (darker contrast) in magnetite; **b** HRTEM image of magnetite hosting Al-rich domains (FFT diffraction pattern of the image at the bottom right); **c** HRTEM image of the Al-rich grain boundary between amphibole and magnetite. White arrows on the FFT pattern, performed on the marked rectangle, show a hercynite signal. **d1–d9** HAADF image and TEM-EDS elemental maps of magnetite and amphibole NP. Note: (1) Al-rich rim on the amphibole NP and the Al-rich areas in the magnetite matrix; (2) depletion of Al, Ti, V, Mn, and Zr concentrations in the amphibole NP
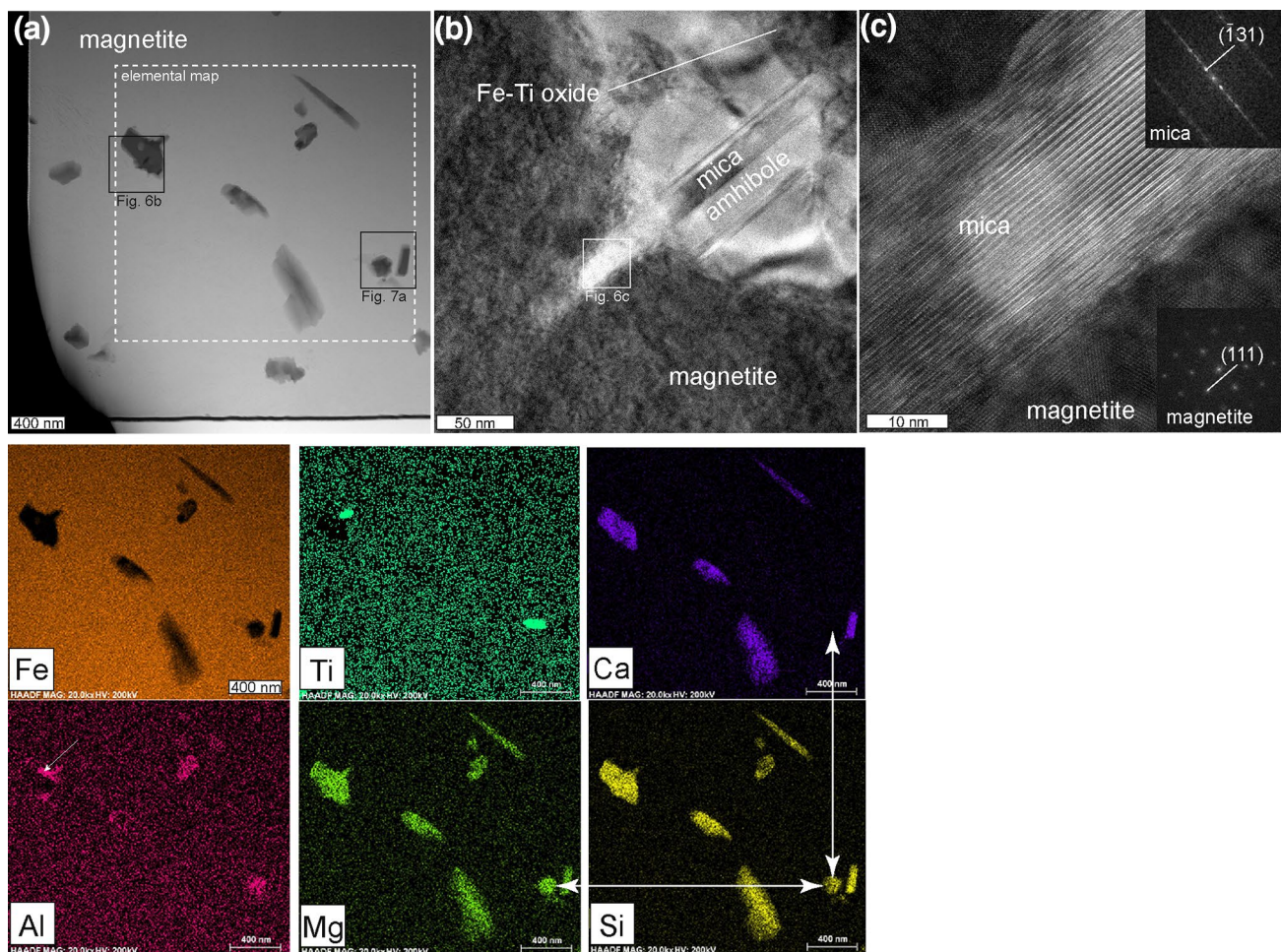
Fig. 6 HAADF-STEM and HRTEM images of inclusions in magnetite and TEM-EDS elemental maps. **a** Low-magnification HAADF-STEM image of a trace element-rich zone containing mineral NPs. **b** BFTEM image of the aggregates of mineral NPs consisting of amphibole, Ti-rich NPs, and elongated mica (phlogopite). **c** HRTEM image of mica inclusions and magnetite associated with FFT patterns. Note: (1) similar distribution of Mg and Si in the NPs, but Ca (double arrowhead white arrows); (2) the heterogeneous concentration of Al around mineral NPs, (3) Ti-rich NPs associated with silicate NPs

Colorados. Knipping et al. (2015b) reported inclusions of actinolite or clinopyroxene (cpx), titanite, and an unspecified Mg–Al–Si-phase in primary magnetite from Los Colorados, which may be trapped in magnetite due to coalescence of several microlites of igneous magnetite. However, this process is highly unlikely to operate during formation of the hydrothermal magnetite characterized by continuous oscillatory zoning in the single crystal of magnetite, with no relicts of the pre-existing microlites (Fig. 2).

Similarly to clinoenstatite, diopside occurs only as individual NPs in the late hydrothermal magnetite (Fig. 6a–c). The euhedral shape of the diopside NPs suggests that it grew contemporaneously with the magnetite surface front (Fig. 7a). Inclusions of diopside in magnetite were reported from numerous deposits including the El Laco IOA in northern Chile (Velasco et al. 2016), and Fe skarn deposits (e.g., Zhao and Zhou 2015). In the latter case, diopside inclusions

formed during the prograde stage of mineralization, while phlogopite co-crystallized with the major stage of magnetite. The relatively rare occurrence of phlogopite in nanoparticulate mineral aggregates at Los Colorados and lack of associated fracturing, suggests that it formed due to local crystallization from entrapped fluid inclusions. However, precipitation of phlogopite along microfractures or smaller scale discontinuities capable of transporting hydrous fluid cannot be ruled out (Sitzman et al. 2000).

The concentration of Ti in magnetite is < 0.3 wt% by EPMA (supplementary data), which is consistent with the less precise (0.2 wt%) obtained by TEM-EDS (Table 2). The TEM-EDS analyses indicate that the concentration of Ti in oxide NPs is variable and ranges from 16 wt%, which is close to the composition of ulvöspinel, to 6.2 wt%, which corresponds to Ti-rich magnetite, and down to 0.2 wt% in the magnetite matrix. The exsolution of ulvöspinel from

Fig. 7 Bright-field, low-magnification TEM images of NPs in magnetite (**a, b, e**); **b, d, f** and **h** have insets displaying FFT pattern generated by fast Fourier transformation of the high-resolution image. **b** HRETM image of grain boundary between diopside and magnetite-(Z); **d** HRETM image of twinned clinoenstatite; **f** HRETM image of Ti-rich particle. **g, h** HRTEM images of amphibole; partial amorphization due to exposure to the electron beam
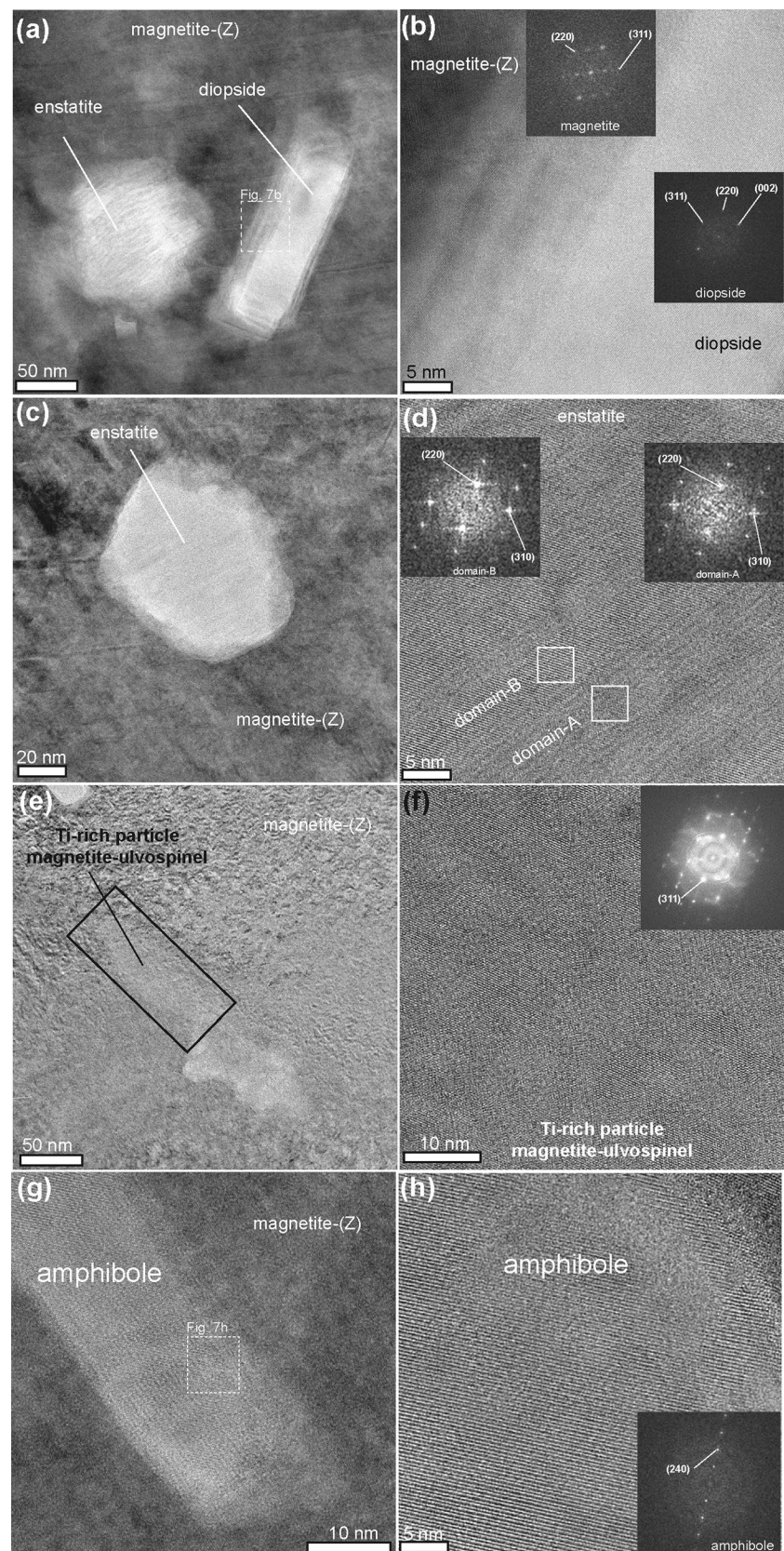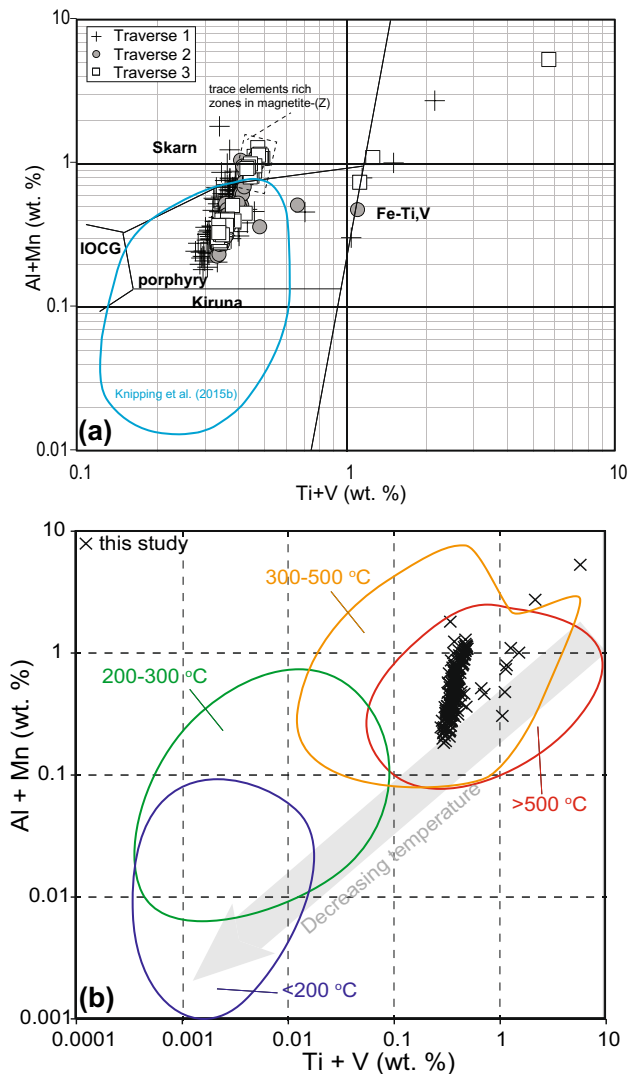
Fig. 8 a, b [Al+Mn] vs. [Ti+V] plots (in wt%) for analyses of magnetite-(X–Z) from Los Colorados. **a** Note that: (1) the majority of magnetite compositions plot in the porphyry and skarn fields; (2) the trace element-rich zones of magnetite-(Z) cluster in the skarn field, whereas the compositions of trace element-poor zones occur in the porphyry field. **b** Note that the distribution of analyses in the field of high-temperature magnetite > 300–500 °C <link rid="credit">(diagrams **a** and **b** modified after Dupuis and Beaudoin (2011) and Nadoll et al. (2014), respectively)

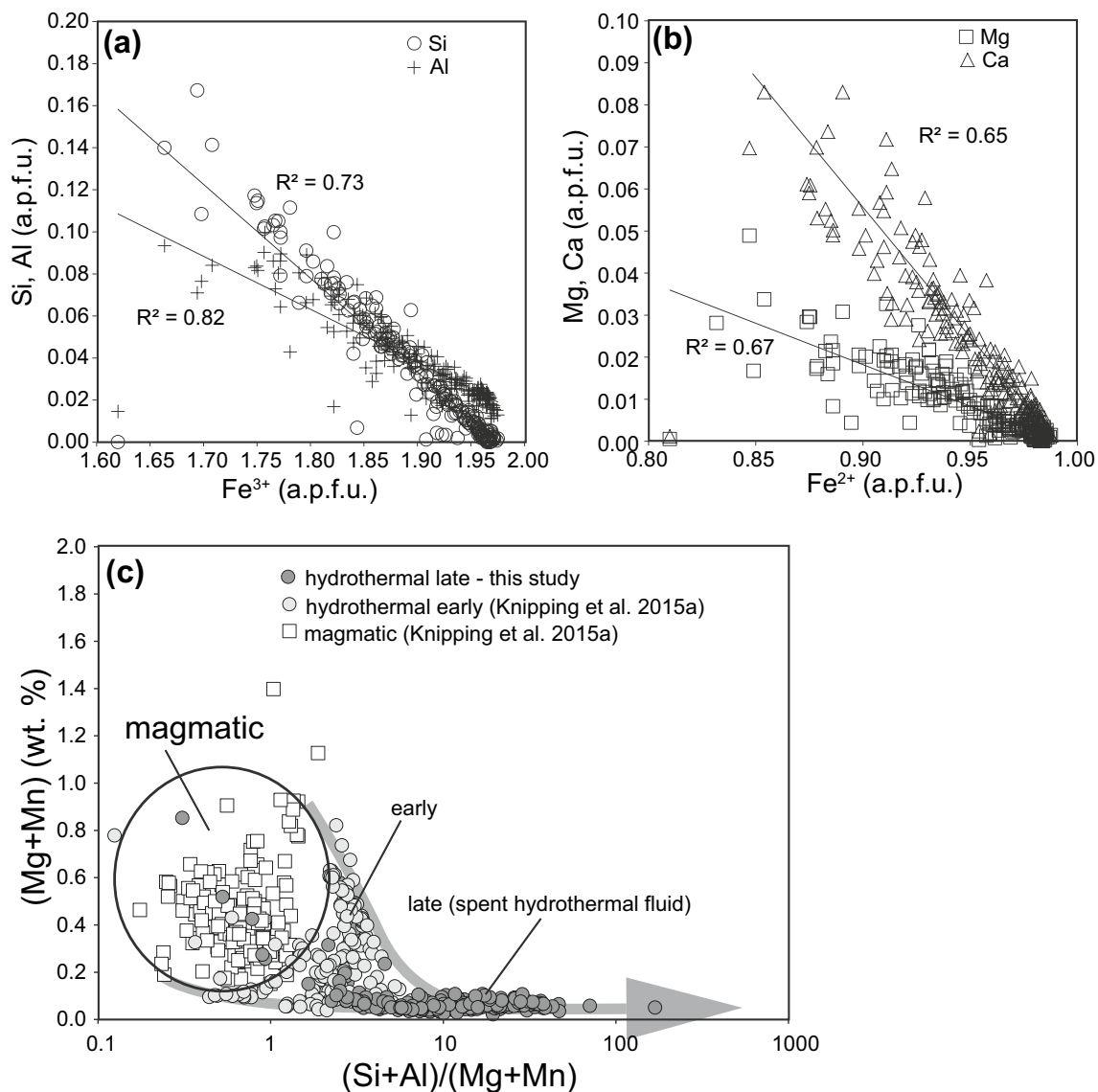the formation of (Fe,Ti)-NPs (von Grunewaldt et al. 1985, and references therein).

The high-resolution observations and analyses revealed that mineral NPs in magnetite from Los Colorados formed by the following mechanisms: (1) crystallization of diopside and clinoenstatite NPs due to local supersaturation of a hydrothermal fluid (with or without contact with the magnetite surface), followed by entrapment during continuous growth of magnetite; (2) local crystallization from the trapped fluid inclusions, as documented by a coexistence of amphibole and phlogopite (Fig. 6); and (3) exsolution of Al-rich domains and Ti-rich NPs from the unstable trace element-rich magnetite host. The mineral NPs would form due to substantial elastic strain energy released as a result of increasing trace element incorporation into the same zone/area of the magnetite crystal. The lack of identifiable porosity in the vicinity of the NPs suggests that dissolution–reprecipitation reactions did not play a major role during their precipitation (e.g., Putnis 2009).

The presence of mineral NPs in the trace element-rich zones in magnetite has important implications for the interpretation of trace element data measured using microbeam techniques such as EPMA or LA-ICP-MS. For example, the studied magnetite displays some well-defined elemental trends (Table 2), most notably an antithetic correlation of Si and Al with Fe^{3+} (Fig. 9). This trend would normally be interpreted to reflect the substitution of Fe^{3+} by Al and Si within the magnetite structure (Hu et al. 2014b). However, it is clearly demonstrated that such interpretation is valid only if no (Si,Al)-bearing nanoparticles are present within the magnetite matrix (Figs. 4, 5). In the Los Colorados magnetite, aluminium forms irregular nanodomains (Fig. 5) within a single crystal of magnetite, and it also occurs as a dissolved element (solid solution) within magnetite nanodomains (Fig. 4d), suggesting that mechanisms of incorporation are varied and complex. Similarly, correlation of Si with divalent cations such as Mg and Ca does not always point to solid solution incorporation as charge balance suggests (Hu et al. 2014b), but instead may point to the presence of (Mg,Ca)-silicates NPs, such as diopside hosted by the magnetite (Figs. 5, 6). Consequently, we argue that elemental correlations alone do not justify conclusions about the mechanisms of trace element incorporation into the magnetite structure.

Concluding remarks

Ore deposits are natural factories for mineral NPs, which form during all stages of mineralization. While homogeneous distribution of trace elements in minerals provides the best opportunity for the successful interpretation of their origin and subsequent evolution, lack of nanoscale information

magnetite occurs below 600 °C, although the presence of trace elements may lower the exsolution temperature to ~ 500 °C (von Grunewaldt et al. 1985 and references therein). No ilmenite was found in the analysed samples, which differs from the magnetite crystallized from the fractionating sulphide liquid (Dare et al. 2012). Therefore, it is suggested that ulvöspinel and Ti-rich magnetite NPs exsolved from the magnetite structure as a result of decreasing solubility of the trace elements. Lack of ilmenite NPs indicates that exsolution and oxidation processes are not a dominant process of

Fig. 9 **a, b** Plots displaying negative correlations between **a** Si and Al vs. calculated Fe^{3+} in atom per formula unit (a.p.f.u.) and **b** Mg and Ca vs. Fe^{2+} (a.p.f.u.). **c** (Mg + Mn) (in wt%) vs. (Si + Al)/(Mg + Mn) plot showing change of the magnetite composition from magmatic (Mg, Mn)-rich to hydrothermal oscillatory-zoned magnetite enriched with Si and Al

about their mineralogical and crystal-chemical form may lead to the misinterpretation of the mechanisms of trace element incorporation and their significance in the formation of ore deposits. The presence of nanoparticulate silicates and oxides in zoned magnetite from the Los Colorados IOA deposit in Chile strongly suggests that similar nanophases are common in zoned oxides, even if WDS elemental mapping displays homogeneous distribution of trace elements (Deditius et al. 2011). In such cases, application of TEM techniques can shed new light into the incorporation of trace elements in magnetite, and provide further information on the physico-chemical processes operating during mineralization. This study documents that processes such

as supersaturation from a hydrothermal fluid or exsolution from the mineral matrix might be responsible for the formation of mineral NPs during continuous growth of magnetite. The alternate, or oscillating, sequence of trace element-rich and trace element-poor growth zones in magnetite, studied here, provides new evidence of abrupt changes in the chemical composition of the mineralizing fluids, previously noted for other minerals, including pyrite (Deditius et al. 2009, 2011; Reich et al. 2013; Tardani et al. 2017). The EPMA analyses and TEM observations clearly demonstrate that partitioning of trace elements into hydrothermal magnetite is modulated by a delicate balance between equilibrium conditions favouring solid-solution incorporation, and kinetic

factors that favour mineral nanoparticle growth. Hence, the presence of mineral NPs vs. solid solution incorporation in the growth zones of magnetite may help interrogate with increased resolution the fluctuating nature of ore forming processes, not accessible otherwise.

These results prove that nanoscale investigations provide a new and very important avenue to elucidate the mechanisms operating during formation of ore deposits as well as to place valuable constraints on the post-depositional changes of ore minerals. Undoubtedly, high-resolution studies of minerals enriched with trace elements are essential when interpreting micro-analytical datasets of minerals.

References

Arato R, Audetat A (2016) Experimental calibration of a new oxybarometer for silicic magmas based on vanadium partitioning between magnetite and silicate melt. Geochim Cosmochim Acta 209:284–295

Arato R, Audetat A (2017) Vanadium magnetite-melt oxybarometry of natural, silicic magmas: a comparison of various oxybarometers and thermometers. Contrib Miner Petrol 172:52

Armstrong JT (1988) Quantitative analysis of silicates and oxide minerals: Comparison of Monte-Carlo, ZAF, and Phi-Rho-Z procedures. Microbeam Analysis, pp 239–246

Bilenker LD, Simon AC, Reich M, Lundstrom CC, Gajos N, Bindeman I, Barra F, Munizaga R (2016) Fe–O stable isotope pairs elucidate a high-temperature origin of Chilean iron oxide-apatite deposits. Geochim Cosmochim Acta 177:94–104

Bosi F, Hålenius U, Skogby H (2009) Crystal chemistry of the magnetite-ulvöspinel series. Am Mineral 94:181–189

Boutroy E, Dare SAS, Beaudoin G, Barnes S-J, Lightfoot P (2014) Magnetite composition in Ni–Cu–PGE deposits worldwide: application to mineral exploration. J Geochem Exp 145:64–81

Buddington AF, Lindsley DH (1964) Iron-titanium oxide minerals and synthetic equivalents. J Petrol 5:310–357

Charlier B, Namur O, Bolle O, Latypov R, Duchesne J-C (2015) Fe–Ti–V ore deposits associated with Proterozoic massif-type anorthosites and related rocks. Earth Sci Rev 141:56–81

Ciobanu CL, Cook NJ, Utsunomiya S, Pring A, Green L (2011) Focussed ion beam-transmission electron microscopy applications in ore mineralogy: bridging micro-and nanoscale observations. Ore Geol Rev 42:6–31

Colás V, Padrón-Navarta JA, González-Jiménez J-M, Griffin WL, Fanlo I, O'Reilly SY, Geervilla F, Proenza JA, Pearson NJ, Escayola MP (2015) Compositional effects on the solubility of minor and trace elements in oxide spinel minerals: insights from crystal-chemical partition coefficients in chromite exsolution. Am Mineral 101:1360–1372

Connoly HC Jr, Burnett DS (2003) On type B CAI formation: experimental constraints on fO_2 variations in spinel minor element partitioning and reequilibration. Geochim Cosmochim Acta 67:4429–4434

Dare SAS, Barnes S-J, Beaudoin G (2012) Variation in trace element content of magnetite crystallized from a fractionating sulphide liquid, Sudbury, Canada: Implications for provenance discrimination. Geochim Cosmochim Acta 88:27–50

Dare SAS, Barnes S-J, Beaudoin G, Méric J, Boutroy E, Potvin-Doucet C (2014) Trace elements in magnetite as petrogenetic indicators. Miner Dep 49:785–796

Dare SAS, Barnes S-J, Beaudoin G (2015) Did the massive magnetite "lava flows" of El Laco (Chile) form by magmatic or hydrothermal processes? New constraints from magnetite composition by LA-ICP-MS. Miner Dep 5:607–617

Davis KJ, Dove PM, De Yoreo JJ (2000) The role of Mg^{2+} as an impurity in calcite growth. Science 290:1134–1137

Deditius AP, Utsunomiya S, Ewing RC, Chryssoulis SL, Venter D, Kesler SE (2009) Decoupled geochemical behaviour of As and Cu in hydrothermal systems. Geology 37:707–710

Deditius AP, Kesler SE, Utsunomiya S, Reich M, Ewing RC (2011) Structural and chemical discontinuities in pyrite. Let's talk of ore deposits, vols I and II, pp 258–260

Dobrzhinetskaya LF, Wirth R, Rhede D, Liu Z, Green HW (2009) Phlogopite and quartz lamellae in diamond-bearing diopside from marbles of the Kokchetav massif, Kazakhstan: exsolution or replacement reaction? J Metamorph Geol 27:607–620

Donovan JJ, Tingle TN (1996) An improved mean atomic number correction for quantitative microanalysis. J Microsc 2:1–7

Donovan JJ, Snyder DA, Rivers ML (1993) An improved interference correction for trace element analysis. Microbeam Anal 2:23–28

Donovan JJ, Singer JW, Armstrong JT (2016) A new method for fast trace element analysis in simple matrices. Am Mineral 101:1839–1853

Dupuis C, Beaudoin G (2011) Discrimination diagrams for iron oxide trace element fingerprinting of mineral deposit types. Miner Dep 46:319–335

Gaspar JC, Wyllie PJ (1983) Magnetite in carbonates from the Jacupiranga Complex, Brazil. Am Mineral 68:195–213

Goldschmidt VM (1954) Geochemistry. Oxford University Press, Oxford

Golla-Schindler U, O'Neill HSC, Putnis A (2005) Direct observation of spinodal decomposition in the magnetite-hercynite system by susceptibility measurements and transmission electron microscopy. Am Mineral 90:1278–1283

Günther T, Klemd R, Zhang X, Horn I, Weyer S (2017) In-situ trace element and Fe-isotope studies on magnetite of the volcanic-hosted Zhibo and Chagangnuoer iron ore deposits in the Western Tianshan, NW China. Chem Geol 453:111–127

Guzmics T, Mitchell RH, Szabó C, Berkesi M, Milke R, Abart R (2011) Carbonatite melt inclusions in coexisting magnetite, apatite and monticellite in Kerimasi calciocarbonatite, Tanzania: melt evolution and petrogenesis. Contrib Mineral Petrol 161:177–196

Haggarty SE (2016) Spinel in planetary systems. Am Mineral 101:5–6

Harrison R, Dunin-Borkowski RE, Putnis A (2002) Direct imaging of nanoscale magnetic interactions in minerals. PNAS 99:16556–16561

Heidarian H, Lentz D, Alirazaei S, Peighambari S, Hall D (2016) Using the chemical analysis of magnetite to constrain various stages in the formation and genesis of the Kiruna–type Chadormalu magnetite-apatite deposit, Bafq district, Central Iran. Mineral Petrol 110:927–942

Henderson CMB, Pearce CI, Charnock JM, Harrison RJ, Rosso KM (2016) An X-ray magnetic circular dichroism (XMCD) study of Fe ordering in a synthetic $MgAl_2O_4$–Fe_3O_4 (spinel-magnetite) solid solution series: Implications for magnetic properties and cation site ordering. Am Mineral 100:1373–1388

Hu H, Lentz D, Li L-W, McCarron T, Zhao X-F, Hall D (2014a) Reequilibration processes in magnetite from iron skarn deposits. Econ Geol 110:1–8

Hu H, Li L-W, Lentz D, Ren Z, Zhao X-F, Deng X-D, Hall D (2014b) Dissolution-reprecipitation process of magnetite from the Chengchao iron deposit: Insights into ore genesis and implication for *in-situ* chemical analysis of magnetite. Ore Geol Rev 57:393–405

Huberty JM, Konishi H, Heck PR, Fournelle JH, Valley JW, Xu H (2012) Silician magnetite from the Dales Gorge Member of the Brockman Iron Formation, Hamersley Group, Western Australia. Am Mineral 97:26–37

Ilton ES, Eugster HP (1990) Partitioning of base metals between silicates, oxides, and chloride-rich hydrothermal fluid: part I. Evaluation of data derived from experimental and natural assemblages. In: Spencer RJ, Chou I-M (eds) Fluid mineral interaction: a tribute to H.P. Eugster. The geochemical Society, Special Publications, No. 2, pp 157–169

Klemm DD, Von Grunewaldt G, Henckel J, Dehm R (1985) The geochemistry of titanomagnetite in magnetite layers and their host rocks. Econ Geol 80:1075–1088

Knipping JL, Bilkner LD, Simon AC, Reich M, Barra F, Deditius AP, Lundstrom C, Wälle M, Heinrich CA, Holtz F, Munizaga R (2015a) Trace element distribution in magnetite as key to a new magmatic-hydrothermal model for Kiruna-type iron oxide-apatite deposits. Geochim Cosmochim Acta 171:15–38

Knipping JL, Bilkner LD, Simon AC, Reich M, Barra F, Deditius AP, Lundstrom C, Bindeman I, Munizaga R (2015b) Giant Kiruna-type deposits form by efficient aggregation of magmatic magnetite suspensions. Geology 43:591–594

Kouchi A, Sugawara Y, Kashima K, Sunagawa I (1983) Laboratory growth of sector zoned clinopyroxenes in the system $CaMgSi_2O_6$-$CaTiAl_2O_6$. Contrib Mineral Petrol 83:177–184

Liu P-P, Zhou M-F, Chen WT, Boone M, Cnudde V (2014) Using multiphase solid inclusions to constrain the origin of the Baima Fe–Ti–(V) oxide deposit, SW China. J Petrol 55:951–976

Nadoll P, Mauk JL, Hayes TS, Koenig AE, Box SE (2012) Geochemistry of magnetite from hydrothermal ore deposits and host rocks of Mesoproterozoic Belt Supergroup, United States. Econ Geol 107:1275–1292

Nadoll P, Angerrer T, Mauk JL, French D, Walshe J (2014) The chemistry of hydrothermal magnetite: a review. Ore Geol Rev 61:1–32

Nadoll P, Mauk JL, Hayes TS, Koenig AE, Box SE (2017) Element partitioning in magnetite under low-grade metamorphic conditions—a case study from the Proterozoic Belt Supergroup, USA. Eur J Mineral 29:795–805

Neumann E-R, Svensen HH, Polozov AZ, Hammer Ø (2017) Formation of Si-Al-Mg-Ca-rich zoned magnetite and end-Permian phretomagmatic pipe in the Tunguska Basin, East Siberia. Miner Dep. https://doi.org/10.1007/s00126-017-0717-9

Newberry NG, Peacor DR, Essene EJ, Geissman JW (1982) Silicon in magnetite: high resolution microanalysis of magnetite-ilmenite intergrowths. Contrib Mineral Petrol 80:334–340

Papike JJ, Purger PV, Bell AS, Shearer CK, Le L, Jones J (2015) Normal to inverse transition in martian spinel: understanding the interplay between chromium, vanadium, and iron valence state partitioning through a crystal-chemical lens. Am Mineral 100:2018–2025

Price GD (1981) Subsolidus phase relations in the titanomagnetite solid solution series. Am Mineral 66:751–758

Putnis A (2009) Mineral replacement reactions. Rev Mineral Geochem 70:87–124

Putnis A, Fernandez-Diaz L, Prieto M (1992) Experimentally produced oscillatory zoning in the $(Ba,Sr)SO_4$ solid solution. Nature 358:743–745

Reguir EP, Chakhmouradian AR, Halden NM, Yang P, Zaitsev AN (2008) Early magmatic and reaction induced trends in magnetite from the carbonatites of Kerimasi, Tanzania. Can Mineral 46:879–900

Reich M, Deditius A, Chryssoulis S, Li J-W, Ma C-Q, Parada MA, Barra F, Mittermayr F (2013) Pyrite as a record of hydrothermal fluid evolution in a porphyry copper system: a SIMS/EPMA trace element study. Geochem Cosmochim Acta 104:42–62

Reich M, Simon AC, Deditius A, Barra F, Chryssoulis S, Lagas G, Tardani D, Knipping J, Bilenker L, Sánchez-Alfaro P, Roberts MP, Munizaga R (2016) Trace element signature of pyrite from the Los Colorados iron oxide-apatite (IOA) deposit, Chile: a missing link between Andean IOA and IOCG systems? Econ Geol 111:743–761

Rodgers DR, Arnott RJ, Wold A, Goodenough JB (1963) The preparation and properties of some vanadium spinels. Phys Chem Solids 24:347–360

Shore M, Fowler AD (1996) Oscillatory zoning in minerals: a common phenomenon. Can Mineral 34:1111–1126

Shtuckenberg AG, Punin YO, Artamova OI (2009) Effect of crystal composition and growth rate on sector zoning in solid solutions grown from aqueous solutions. Mineral Mag 73:385–398

Sievwright RH, Wilkinson JJ, O'Neil HSC, Berry AJ (2017) Thermodynamic controls on element partitioning between titanomagnetite and andesitic–dacitic silicate melts. Contrib Mineral Petrol 172:62

Sitzman SD, Banfield JF, Valley JW (2000) Microstructural characterization of metamorphic magnetite crystals with implications for oxygen isotope distribution. Am Mineral 85:14–21

Sossi PA, Prytulak J, O'Neill HSC (2018) Experimental calibration of vanadium partitioning and stable isotopes fractionation between hydrous granitic melt and magnetite at 800 °C and 0.5 GPa. Contrib Mineral Petrol 173:27

Stowell H, Zuluaga C, Boyle A, Bulman G (2011) Garnet sector and oscillatory zoning linked with changes in crystal morphology during rapid growth, North Cascades, Washington. Am Mineral 96:1354–1362

Tardani D, Reich M, Deditius AP, Chryssoulis S, Sánchez-Alfaro P, Wrage J (2017) Cu–As decoupling in an active geothermal system: a link between pyrite and fluid composition. Geochim Cosmochim Acta, 204:179–204

Tauson VL, Smagunov NV, Lipko SV (2017) Cocrystallization coefficients of Cr, V, and Fe in hydrothermal ore systems (*from experimental data*). Russ Geol Geophys 58:949–955

Toplis M, Corgne A (2002) An experimental study of element partitioning between magnetite, clinopyroxene and iron-bearing silicate liquid with particular emphasis on vanadium. Contrib Mineral Petrol 144:22–27

Utsunomiya S, Ewing RC (2003) Application of high-angle annular dark field scanning transmission microscopy, scanning transmission electron microscope-energy dispersive X-ray spectrometry, and energy-filtered transmission electron microscopy to the characterization of nanoparticles in the environment. Environ Sci Technol 37:786–791

Velasco F, Tornos F, Hanchar FM (2016) Immiscible iron- and silica-rich melts and magnetite geochemistry at the El Laco volcano (northern Chile): evidence for a magmatic origin for the magnetite deposits. Ore Geol Rev 79:346–366

von Grunewaldt G, Klemm DD, Henckel J, Dehm RM (1985) Exsolution features in titanomagnetite from massive magnetite layers and their host rocks of the Upper Zone, Eastern Bushveld Complex. Econ Geol 80:1049–1061

Wang YG, Ye HQ, Ximen LL, Kuo KH (1989) A HRTEM study of the intergrowth of magnetite and coulsonite. Acta Crystallogr A45:264–268

Watson EB (1996) Surface enrichment and trace-element uptake during crystal growth. Geochim Cosmochim Acta 60:5013–5020

Watson EB (2004) A conceptual model for near-surface kinetic controls on the trace-element and stable isotope composition of abiogenic calcite crystals. Geochim Cosmochim Acta 68:1473–1488

Watson EB, Liang Y (1995) A simple model for sector zoning in slowly grown crystals: implications for growth rate and lattice diffusion, with emphasis pm accessory minerals in crystal rocks. Am Mineral 80:1179–1187

Weinbruch S, Styrsa V, Müller WF (2003) Exsolution and coarsening in iron-free clinopyroxene during isothermal annealing. Geochim Cosmochim Acta 67:5071–5082

Xie Q, Zhang Z, Hou T, Jin Z, Santosh M (2017) Geochemistry and oxygen isotope composition of magnetite from the Zhangmatun deposit, North China: Implications for the magmatic-hydrothermal evolution of Cornwall-type iron mineralization. Ore Geol Rev 88:57–70

Xu H, Shen Z, Konishi H (2014) Si-magnetite nano-precipitates in silician magnetite from banded iron formation: Z-contrast imaging and ab initio study. Am Mineral 99:2196–2202

Yang Y-L, Ni P, Wang G-G, Xu Y-F (2017) Constraints on the mineralization processes of the Makeng iron deposit, eastern China: fluid inclusion, H-O isotope and magnetite trace element analysis. Ore Geol Rev 88:791–808

Zhao WW, Zhou M-F (2015) In-situ LA-ICP-MS trace elemental analysis of magnetite: the Mesozoic Tengite skarn Fe deposit in the Nanling Range, South China. Ore Geol Rev 65:872–883